

Microstructure and Wear Resistance of ZrC-ZrB₂/Ni Composite Coatings Prepared by Plasma Transferred Arc Cladding

Tian-guo Guan^a, Mei-qing Cao^{a*}, Kun Xie^a, Xiao Lv^a, Yun-liang Tan^b

^aCollege of Material Science and Engineering, Shandong University of Science and Technology, Qingdao 266590, China

^bState Key Laboratory of Mining Disaster Prevention and Control Co-founded by Shandong Province, Ministry of Science and Technology, Shandong University of Science and Technology, Qingdao 266590, China

Received: December 01, 2018; Revised: February 19, 2019; Accepted: March 28, 2019

The ZrC-ZrB₂/Ni metal matrix composite coatings were in-situ synthesized from a mixture of Ni, Zr and B₄C by plasma transferred arc (PTA) cladding process. Microstructures and phase constituents of the coatings were characterized by electron probe micro-analyzer (EPMA) and X-ray diffraction (XRD). Microhardness and wear resistance of the coatings were systematically investigated by means of vickers hardness tester and wear tester. The results showed that the main phases of the composite coatings were ZrB₂ and ZrC. The coatings had a sound metallurgical bonding to the SA-283C steel substrate. Microhardness and wear resistance of the substrate were greatly improved by the composite coatings, and both of them showed a tendency to increase first and then decrease with the increase of the Ni content. As the content of Ni was 30 wt.%, the hardness of the coating reached the maximum value, 1522 HV, and the wear resistance was about 15 times that of the substrate.

Keywords: PTA cladding, ceramic, coating, microstructure, tribology.

1. Introduction

It is one of the most effective ways of using coatings to improve the surface properties¹. Metal matrix composite (MMC) coatings reinforced by ceramic particulates have superior mechanical properties and excellent wear resistance, and they can combine the properties of ductile metallic matrix and a hard ceramic reinforcement, which makes them become the promising candidates of advanced engineering structure materials.

A variety of ceramic particulates can be selected as the reinforcements, such as borides, nitrides, carbides, and oxides^{2,3}. Among the ceramic reinforcements, refractory materials ZrC and ZrB₂ have many desirable properties, such as high hardness, ultrahigh melting point, high-thermal stability and excellent wear resistance⁴⁻⁸. Due to their inherent advantages, these ceramic phases are attractive as wear resistance systems and cutting tools.

In the previous work, metal matrix composite coatings have been produced by several methods, such as laser cladding, plasma cladding, atmospheric plasma spraying technique⁹⁻¹³. Zhang et al.⁹ synthesized TiC-TiB₂/Cr coating on a T61206(UNS) steel by using laser surface engineering, and the results showed that the wear resistance and high temperature oxidation resistance of the coatings were greatly improved compared with the 5CrNiMo steel. Xu et al.¹⁰ prepared a ZrB₂-ZrC reinforced Ni-based composite coating on the surface of magnesium alloy by an

atmospheric plasma spraying technique. The APS coatings had better wear resistance than that of the substrate. Zhang et al.¹¹ developed a multiple ceramic particulates reinforced Fe-based alloy composite coating by PTA cladding process. This composite coating significantly enhanced the hardness and wear resistance of the substrate.

Among these deposition techniques, PTA cladding process is widely used on account of the extremely high temperature, convenient operation and low cost¹⁴. In addition, dense coatings with good metallurgical bonding to substrates can be fabricated by PTA cladding rather than the mechanical bonding produced by an atmospheric plasma spray. In addition, the in-situ synthesis is being used to produce composite coatings in view of the outstanding interfacial compatibility between matrices and reinforcements.

In this investigation, the ZrB₂-ZrC/Ni cermet coatings were in-situ synthesized by PTA cladding with a mixture of Ni, Zr and B₄C. The influence of the Ni content in the coatings on the microstructure and wear resistant properties was studied.

2. Experimental Procedure

The SA-283C steel plate with the dimensions of 120 mm x 40 mm x 10 mm was used as substrate material. The chemical composition of the substrate in wt.% was: 0.17 C, 0.14 Mn, 0.35 Si, 0.03 S and 0.03 P with the rest of Fe. The starting materials used were commercial powders of Ni (20-45 μm, purity 99.0%), Zr (9-39 μm, purity 99.0%) and B₄C (24-75 μm, purity 95.0%). The Ni powder was added

*e-mail: cmqlysh2006@126.com

into the $3\text{Zr-B}_4\text{C}$ (mole ratio) powders in different ratio with Ni contents of 10, 30 and 50 wt.%, respectively. The powders were homogenized in a QM-1SP2 planetary ball mill for 4 h at a low speed (≤ 25 rpm) and then preplaced on the substrate with sodium silicate. The thickness of the preplaced layer was about 1.0 mm.

A DRF-2 type PTA cladding equipment designed by Shandong University of Science and Technology was used. The operating principle of the PTA cladding system is schematically shown in Fig.1. To obtain a coating with good bonding, a smooth coating surface and a minimum dilution, the PTA cladding parameters have been optimized and showed in Table 1. The coatings with 10, 30 and 50 wt.% Ni contents in the feedstock powders will be referred to hereafter in terms of sample S1, S2 and S3, respectively.

An X-ray diffraction (XRD) (Rigaku D/Max 2500PC) was used to analyze the phase composition of the coatings with Cu-K α radiation operated at 40 kV and 100 mA. Besides, the scanning rate was 6 $^\circ$ /min and the scanning angle ranged from 20 $^\circ$ to 90 $^\circ$. Microstructure of the coatings was observed by JXA-8230 electron probe micro-analyzer (EPMA) equipped with an energy-dispersive X-ray spectrometer (EDS) to characterize the element distribution.

Microhardness was measured by means of FM-700 Vickers hardness tester with a load of 98 g and loading time of 15 s. All the microhardness value shown in this study was an average of 5 measurements to improve the accuracy. A linear reciprocating tribometer (CETR-UMT-3 Ultra-functional Attrition Testing Machine) was used to measure the friction coefficient of the coatings. The Si_3N_4 ceramic ball (9.525 mm in diameter) has been used as friction counterface

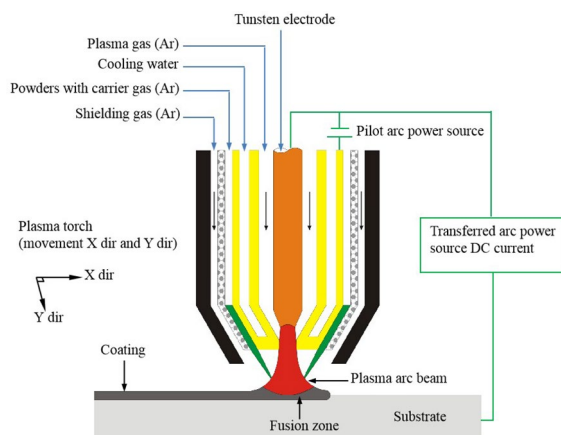


Figure 1. Schematic diagram of the PTA cladding system.

Table 1. Parameters of PTA cladding.

Current(A)	90
Voltage(V)	30
Scanning velocity (mm/min)	600
Plasma gas flow (Ar,m ³ /h)	0.2
Protective gas flow (Ar,m ³ /h)	0.5

whose hardness is approximately 1500 HV. The friction and wear tests were performed at room temperature under a normal load of 50 N with a sliding speed of 10 mm/s, a wear time of 60 min and an amplitude of 6 mm. Wear tests of the coatings without lubricant was carried out by using an M-2000 type wear tester at room temperature and normal atmosphere conditions. A 52100 steel with the hardness of 62 HRC was used as the friction counterpart. The rotating speed and wear time during the wear tests were fixed at 200 rpm and 8 h. Furthermore, the applied load was 200 N. Prior to starting the tests, the surface of the coatings was all ground by metallographic sandpaper and polished using W1.5 diamond grinding paste.

3. Results and Discussion

3.1 Analysis of phase constituents in the coatings

Fig. 2 shows the XRD patterns of the composite coatings. It can be observed that the composite coatings were mainly composed of ZrC and ZrB_2 . This indicates that the chemical reaction between Zr and B_4C occurred during PTA cladding process. In addition, there were a few $\gamma\text{-Ni}$ and ZrO_2 diffraction peaks in the coatings. Although argon gas was used as a shielding gas to minimize surface contamination during the PTA cladding process, a small amount of oxidation still occurred during the PTA cladding process.

3.2 Microstructure of the composite coatings

Fig. 3 shows the cross-sectional views of the composite coatings. It can be found that the coatings are free of cracks and the average thickness of the coatings is approximate 1.2 mm. However, a few pores are visible in the cladding coatings, which could be explained by the encapsulated bubbles generated during the PTA cladding process¹⁵. The bonding zones between the coatings and the substrates are thin bands with planar growth. The crystal structure is governed by the temperature gradient at the solid-liquid interface (G) to the solidification speed (R) ratio. When the G is very high

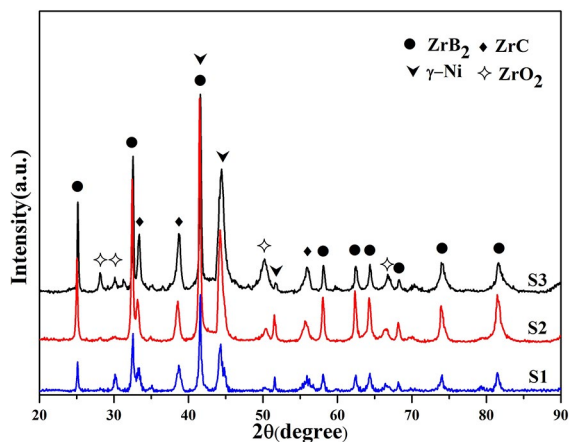


Figure 2. X-ray diffraction patterns of the composite coatings.

and R is very low and the degree of supercooling is close to zero, the growth will be limited. Hence, planar crystal appears in the bonding areas (see Fig. 3b), which indicates the presence of a sound metallurgical joint to the substrate.

The typical EPMA morphologies of the coatings are shown in the Fig. 4. It can be found that there are mainly two kinds of reinforcements with acicular or clubbed and granular structure in the coatings. We can see that the size of dendritic grain of sample S1 is larger than that of other samples. The reason is that the content of Zr and B₄C is very high in sample S1, which is favorable for dendritic grains growth. Under the circumstances, crack defects are easily formed during the growth of the clubbed structure (see Fig. 4a),

which adversely affect the strength of reinforcement phase. Moreover, to establish a clear correspondence between the microstructural features and the phases present, the EDS analysis was performed on the surface of the composite coatings, as shown in Fig. 5. The B-rich phase is correspondence to the clubbed structure, and Zr-rich phase is correspondence to the clubbed and granular structure. In addition, it can be seen that the carbon is distributed all over the selected area except the B-rich regions. Combined the EDS results with the results of XRD analysis, a conclusion can be obtained that these clubbed structure are ZrB₂, and granular structure are ZrC.

The cross-sectional micrographs of the composite coating of sample S2 are exhibited in Fig. 6. It can be found that

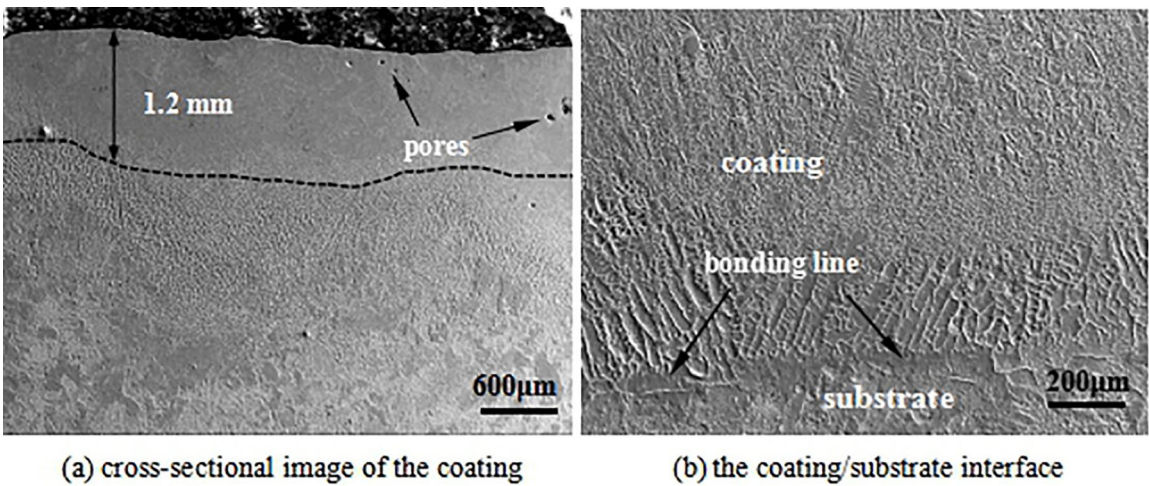


Figure 3. Cross-sectional images of the composite coatings.

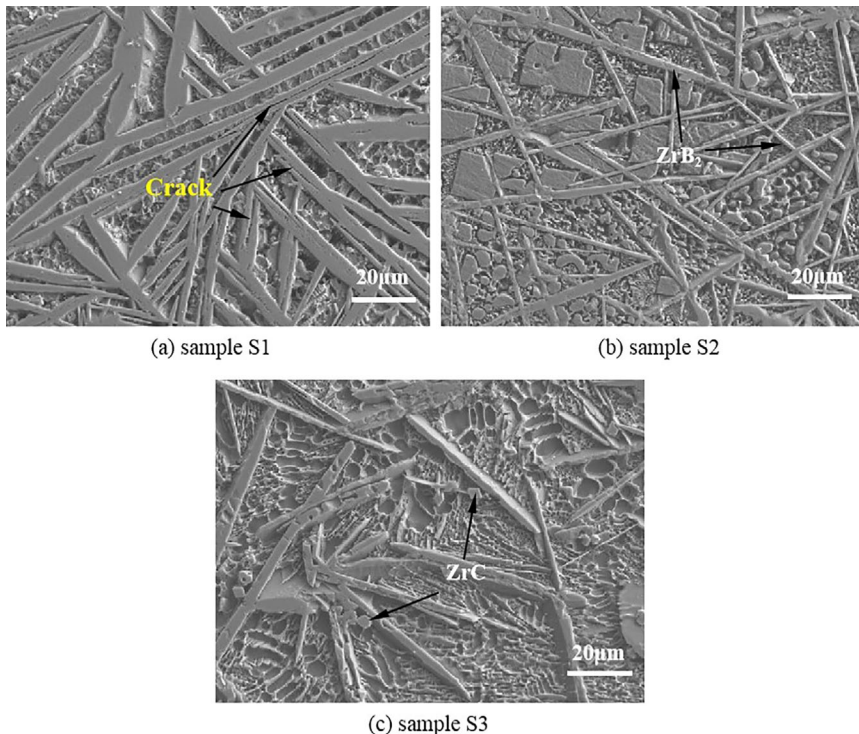


Figure 4. EPMA micrographs of the middle zone of the coatings: (a)sample S1; (b)sample S2; (c)sample S3.

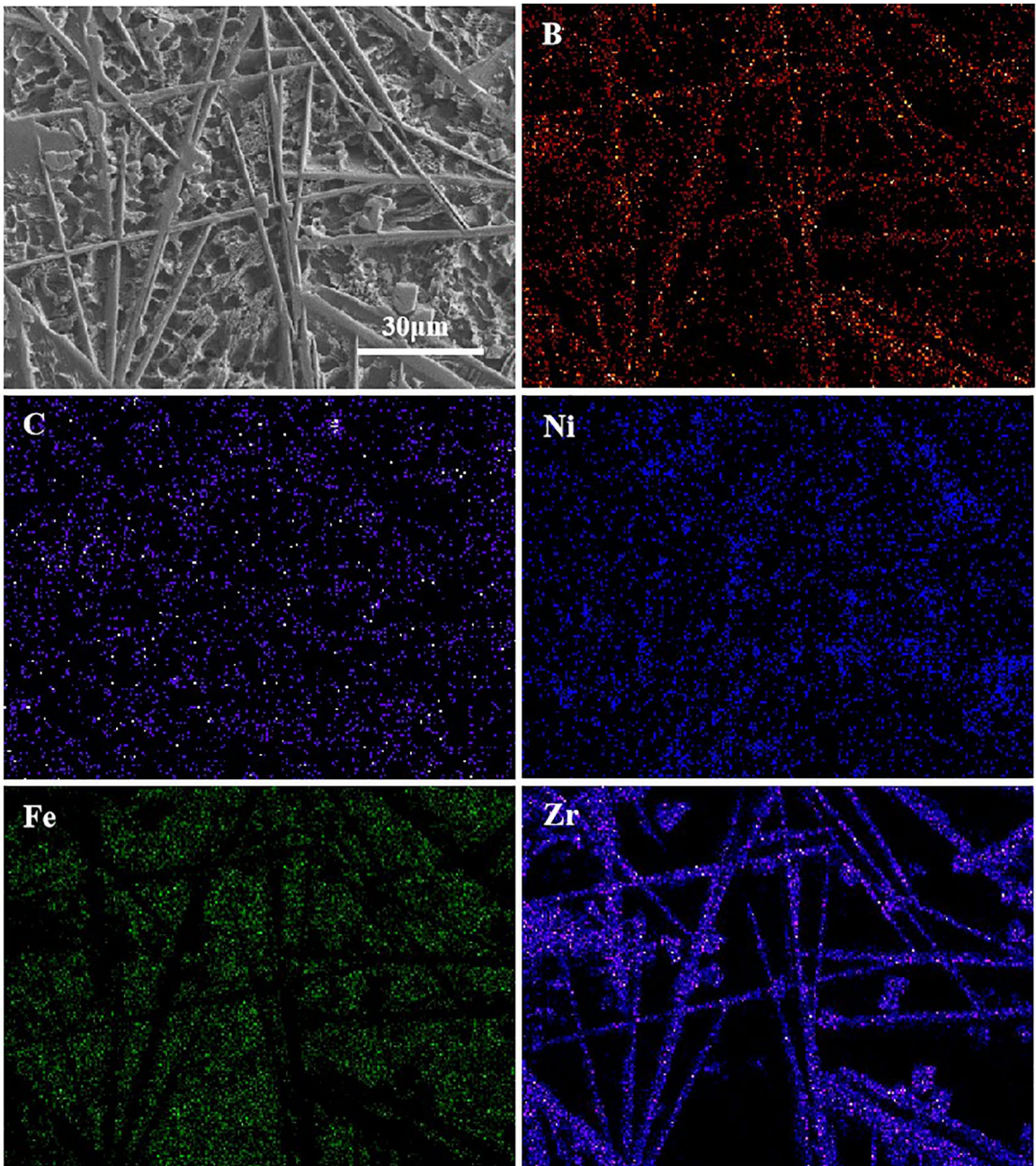


Figure 5. EDS element distribution maps of the composite coating of sample S2.

there are two types of ZrB_2 grains formed in the $Zr-B_4C$ system coating from the top to the bottom. In general, ZrB_2 grains are mainly slender acicular structure on the top of the composite coating and tend to be short clubbed structure at the bottom. The ratio of length and width for ZrB_2 particles decrease significantly, which is similar to the previous study¹⁴.

According to the solidification theory, the grain number in unit volume (Z) is determined by the following equation¹⁶:

$$Z = k \cdot \left(\frac{N}{G} \right)^{\frac{3}{4}} \quad (1)$$

Where, N is nucleation rate; G is the growth rate. When the grains are spherical, K is 0.9. During the PTA cladding process, the surface of the preplaced powder absorbs more heat. As a consequence, the surface temperature of molten pool increases greatly and melting the heterogeneous nucleus.

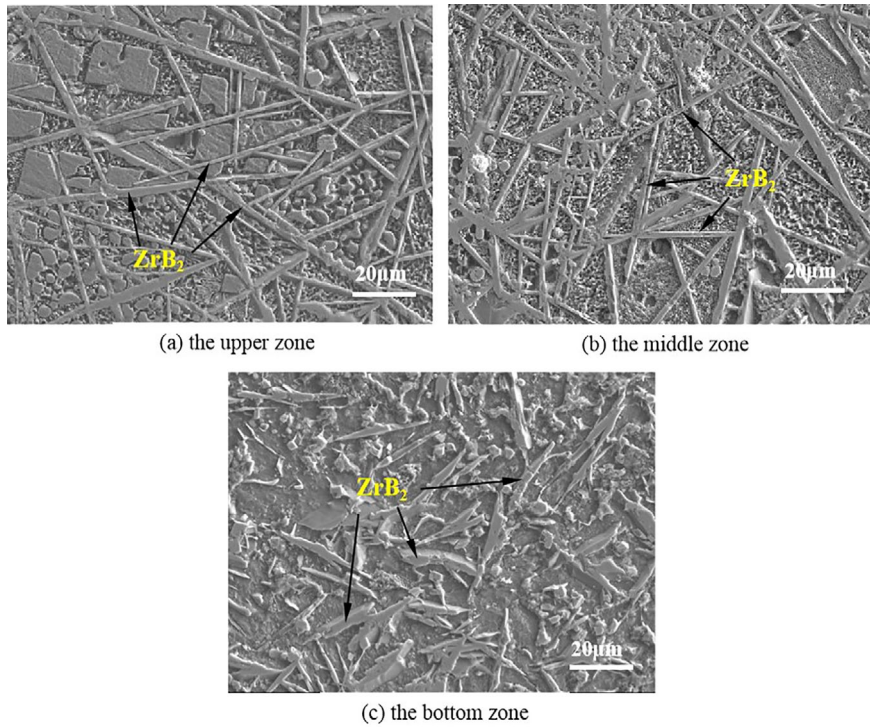


Figure 6. EPMA micrographs of sample S2 with a vertical distribution of reinforcements: (a)the upper zone; (b)the middle zone; (c)the bottom zone.

Therefore, the nucleation rate (N) decreases. In addition, the increase in the surface temperature leads to the increase of grain growth rate (G). As a result, the N/G ratio also goes down. The number of ZrB₂ grains on the upper zone of the composite coating is less than that at the bottom.

In the meantime, due to the mass density of reactants B₄C (2.52 g/cm³) and Zr (6.49 g/cm³) lower than that of the liquid Fe-based metal (about 7.86 g/cm³), the reactants Zr and B₄C are inclined to flow to the upper zone of the molten pool. In addition, the dilution rate on the upper of the cladding layer is smaller than that at the bottom. Under this circumstance, the concentrations of Zr, B and C atoms on the top of the composite coating are much higher than that at the bottom, which is benefit for the continuous growth of ZrB₂ grain. On the contrary, the ZrB₂ grains at the bottom of the coating present clubbed structure. On one hand, the high dilution rate and low cooling rate are harmful to the primary nucleation of ZrB₂ particles¹⁴. Hence, most of the ZrB₂ grains at the bottom of the coating belong to secondary nucleation. On the other hand, the growth time for ZrB₂ grains are prolonged with the increase of dilution rate. As a result, the ZrB₂ phases at the bottom of the coating are eventually coarsened.

3.3 Hardness of the composite coatings

Fig. 7 shows the microhardness curves for the obtained composite coatings along the depth of cross-section. The distinctive high hardness of the composite coating can

be attributed to the high content of ZrC and ZrB₂ ceramic reinforcement phases in the coating. It can be found that the hardness firstly increases, and then decreases gradually with the increase of Ni content. When the Ni addition is 30 wt.%, the average hardness of the coating reaches the maximum value, about 1522 HV. This result is in good agreement with the previous study¹⁰. The results show that the APS composite coating with 30 wt.% Ni content also has the highest hardness value of 525.02 ± 96.08 HV_{0.1}, far below our experimental value. The reason is that the structure of the APS coatings is unconsolidated and porous. As can be seen in Fig.4, the grain size of sample S2 is smaller than that of

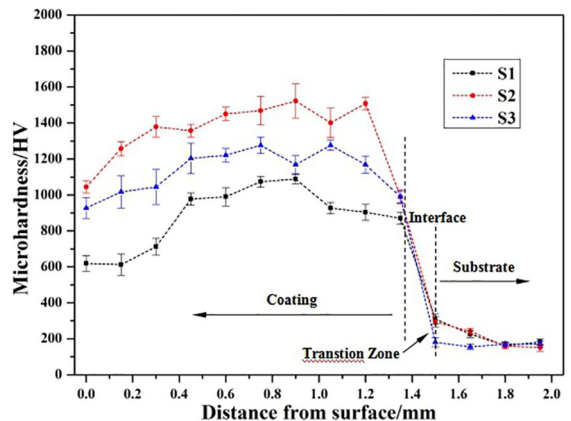


Figure 7. Microhardness profiles across the depth of the composite coatings.

sample S1 and S3. According to the Hall-Petch equation, the Vickers hardness decreases with increasing grain size¹⁷⁻¹⁹. Therefore, the coating with 30 wt.% Ni content possesses the highest hardness among all the samples. It can be noted that hardness value has a gradient distribution from the surface of the coating to the substrate. The reason is that there may be some small slags and impurities in the surface of the coatings. Therefore, the hardness is relatively low²⁰. With the effect of dilution induced by the substrate melting, the hardness of the transition zone decreases remarkably (see Fig. 6).

3.4 Wear resistance of the composite coatings

Fig. 8 shows the wear mass loss of the cladding coatings and the substrate. It can be seen that the wear mass loss of the SA-283C steel substrate is considerably larger than those of composite coatings. The improvement of wear resistance is primarily attributed to the presence of hard reinforcement in the coatings. The refractory ceramic particles of ZrB_2 and ZrC with high hardness can play the role of hard barrier to impede the scratching and ploughing from the abrasive granule, hence, the loss of material is reduced significantly²¹. Besides, the wear resistance of the coatings shows a trend of increasing firstly and then decreasing with an increase in the Ni content, which is consistent with the variation trend of hardness curves (see Fig. 7). When the content of Ni is 30 wt.%, the coating shows the highest wear resistance. The wear mass loss of sample S2 is approximately 1/15 of that of the substrate. The wear resistance of the coatings in this work is significantly better than that of TaC/Ni coatings¹⁵. The reason is that ZrB_2 and ZrC particles can inhibit the growth of each other, resulting in the grain refinement. Thereby, ZrB_2 - ZrC composite ceramic has better properties than the single component ceramic. Furthermore, the hardness of ZrB_2 and ZrC is higher than that of TaC.

The variation of friction coefficients of composite coatings and substrate as a function of time are presented in Fig. 9. It can be seen that the coefficients of friction vary within a range of 0.45 and 0.55 for the composite coatings while friction coefficient of the substrate fluctuates between 0.63 and 0.68. The reason is that the composite coatings which

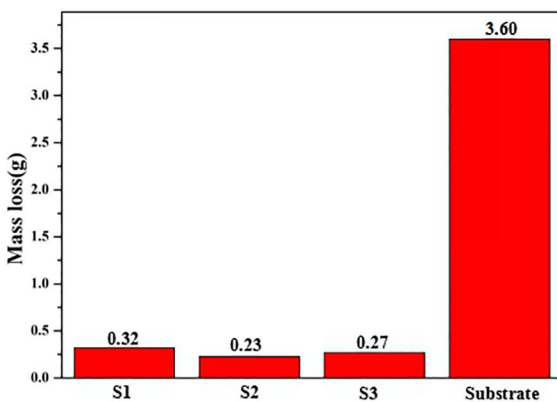


Figure 8. Mass loss of the coatings and substrate.

possess high hardness can avoid plastic deformation when interacting with the counter surface during tribological tests. Therefore, the coatings present relatively small contact areas and correspondingly low friction coefficients in comparison to the substrate²². In addition, we can find that the variation law between the hardness and friction coefficient of the coating, which is that the friction coefficient decreases with the increase of the surface hardness (see Fig. 7). Besides, the surface of the coating may contain some small slags and impurities, which leads to the relatively high friction coefficient in the running-in period.

3.5 Wear mechanisms of the composite coatings

The worn surface morphology is related to the wear mechanism. Fig. 10 shows the worn surface morphologies of the coatings and substrate. It can be seen from Fig. 10a that the worn surface of the substrate is characterized by deep plowing grooves and adhesive craters and severe plastic deformation due to the low hardness of the SA-283C steel substrate, which indicates that the wear mechanism for the substrate is severe abrasive wear and adhesive wear. The worn surfaces of the composite coatings are smooth with only shallow grooves and a few fatigue pits, as shown in Fig. 10. Therefore, it can be considered that the wear mechanism is mixed of abrasive wear and fatigue wear with a small amount of delamination on the worn surface. In addition, the worn surfaces of the composite coatings in this work are smoother than that of APS coatings¹⁰, which can be attributed to the higher microhardness of the coatings in this work than that of APS coatings.

It is well known that the wear resistance of metallic material depends upon several factors, such as volume fraction, distribution of the ceramic particles, and wear condition²³. During friction process, the reinforcements which own high hardness can prevent the abrasive particles from being pressed into the surface of composite coatings. In addition, the ceramic particles can overcome plough-effect by breaking the abrasive particles up and causing them to

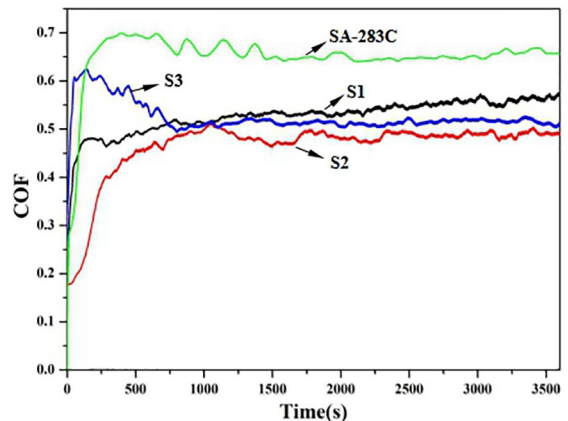


Figure 9. Variation of friction coefficient of the composite coatings and substrate.

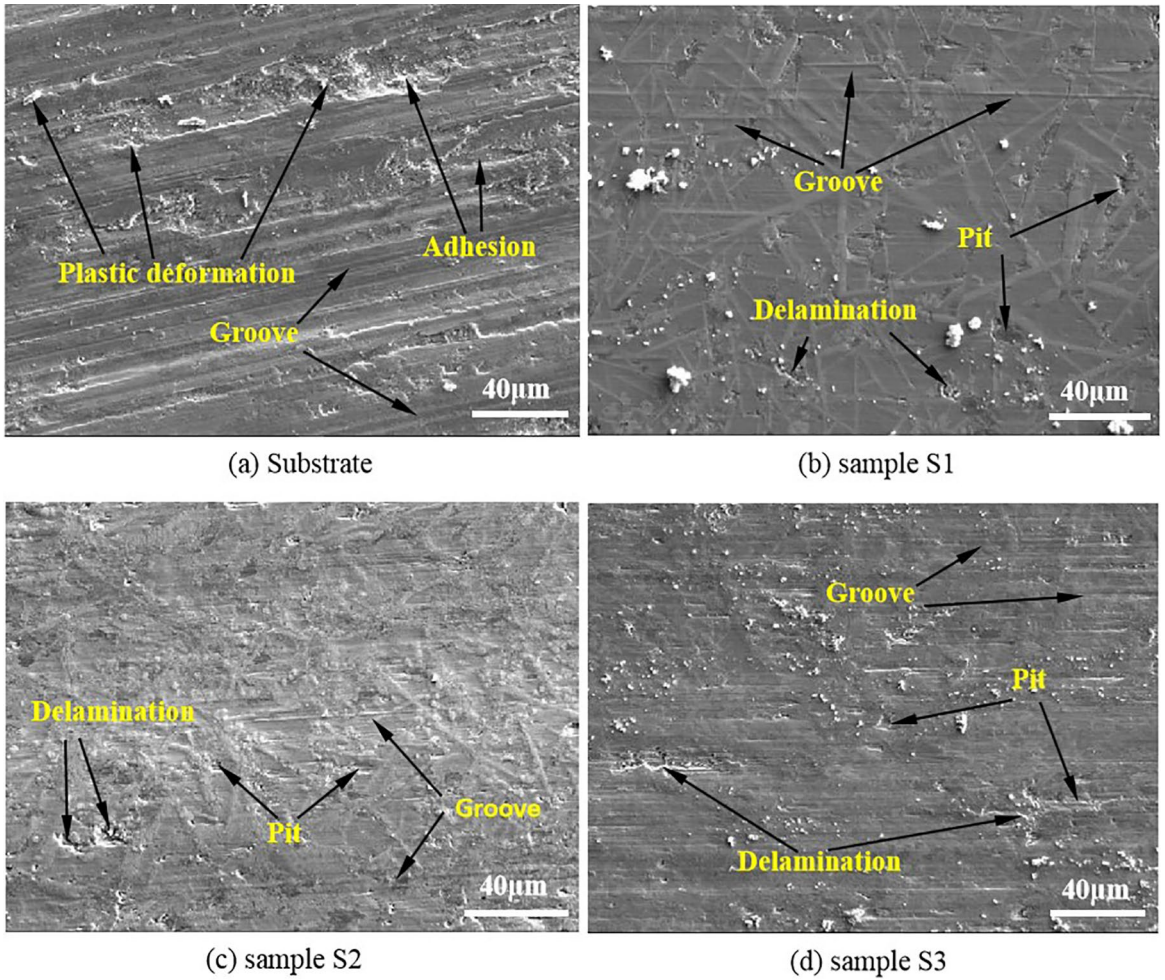


Figure 10. EPMA micrographs of the worn surface morphologies of the coatings and substrate: (a) Substrate; (b) Sample S1; (c) Sample S2; (d) Sample S3.

lose their cutting function. Hence, the worn surfaces are smooth and grooves are shallow and narrow. From the above considerations, it is apparent that improved abrasive wear resistance in this system can be achieved by increasing the volume fraction of reinforcements. However, it can be seen that some irregular debris is present on the worn surface of the low Ni content coating (see Fig. 10b). For the sample S1 with the low binder phase, the ceramic particles can be easily removed from the matrix during the wear process, leading to the formation of debris and craters. This is in agreement with the previous study²⁴. In addition, when the Ni content increases to a certain extent, the ceramic content in the coating decreases and the inhibition effect of the ceramic particles also decreases. Therefore, some continuous and deep grooves are present on the worn surface (see Fig. 10d).

The microstructure also plays a role in determining the mechanism in composite coating, as shown in Fig. 11. In the dry sliding wear process, fatigue cracks form and grow under the effect of the alternating stress. The reinforcements can limit the propagation of fatigue cracks. Under the action

of repeated friction, the ceramic particles break and fall off eventually. This produces some fatigue pits. However, if the ceramic particles are too large, some microcracks are likely to occur during their growth (see Fig. 4a). The strength of the reinforcement phase decreases significantly. Therefore, the reinforcements in sample S1 are more likely to be destroyed. The wear resistance of sample S1 is lower than that of sample S2. In sample S3, due to the low content of reinforcements (see Fig. 4c), microcracks propagate easily, resulting in the formation of peeling pits on the wear surface. The wear resistance decreases subsequently.

4. Conclusions

- (1) The ZrC-ZrB₂ particles reinforced Ni-based composite coatings were fabricated by PTA cladding from a mixture of Ni, Zr and B₄C. The composite coatings showed a sound metallurgical bonding to the substrate. The main phases of the composite coatings were ZrC and ZrB₂. ZrB₂ phase showed

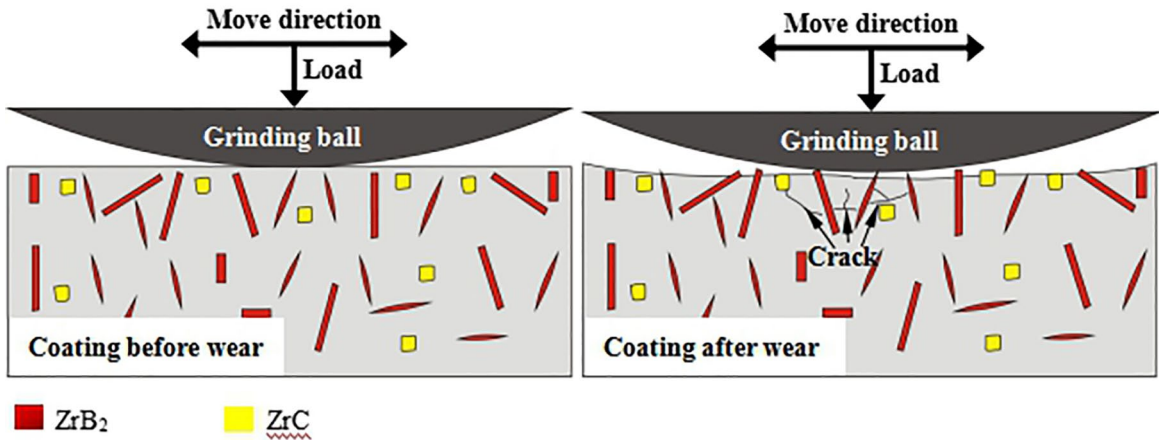


Figure 11. Schematic diagram of abrasive wear mechanism of the coatings.

the acicular or clubbed structure, and ZrC phase present the granular structure in the coatings.

- (2) The hardness of the composite coatings first increased and then decreased with the increase of Ni content. As the content of Ni was 30 wt.%, the coating displayed the highest hardness of 1522 HV as well as the best wear resistance. The wear mass loss of the composite coating is approximately 1/15 of that of the substrate. Furthermore, the worn surface of the composite coatings was relatively smooth, and the wear mechanism was mixed of abrasive wear and fatigue wear.

5. Acknowledgments

This research was supported by National Key R&D Program of China 2018YFC0604703; the Natural Science Foundation of Shandong Province (ZR2018MEM008) and the Project of Shandong Province Higher Educational Science and Technology Program [J17KA019].

6. References

1. Liu P, Shi QY, Zhang YB. Microstructural evaluation and corrosion properties of aluminium matrix surface composite adding Al-based amorphous fabricated by friction stir processing. *Composites Part B: Engineering*. 2013;52:137-143.
2. Anand A, Das M, Kundu B, Balla VK, Bodhak S, Gangadharan S. Plasma-Sprayed Ti6Al4V Alloy Composite Coatings Reinforced with In Situ Formed TiB-TiN. *Journal of Thermal Spray Technology*. 2017;26(8):2013-2019.
3. Masanta M, Shariff SM, Choudhury AR. Evaluation of modulus of elasticity, nano-hardness and fracture toughness of TiB₂-TiC-Al₂O₃ composite coating developed by SHS and laser cladding. *Materials Science and Engineering: A*. 2011;528(16-17):5327-5335.
4. Hu Q, Luo P, Zhang M, Song M, Li J. Combustion and formation behavior of hybrid ZrB₂ and ZrC particles in Al-Zr-B₄C system during self-propagation high temperature synthesis. *International Journal of Refractory Metals and Hard Materials*. 2012;31:89-95.
5. Xu L, Huang C, Liu H, Zou B, Zhu H, Zhao G, et al. Study on in-situ synthesis of ZrB₂ whiskers in ZrB₂-ZrC matrix powder for ceramic cutting tools. *International Journal of Refractory Metals and Hard Materials*. 2013;37:98-105.
6. Guo SQ. Densification, microstructure, elastic and mechanical properties of reactive hot-pressed ZrB₂-ZrC-Zr cermets. *Journal of The European Ceramic Society*. 2014;34(3):621-632.
7. Wu H, Li HJ, Fu QG, Yao DJ, Wang YJ, Ma C, et al. Microstructures and Ablation Resistance of ZrC Coating for SiC-Coated Carbon/Carbon Composites Prepared by Supersonic Plasma Spraying. *Journal of Thermal Spray Technology*. 2011;20(6):1286-1291.
8. King DS, Hilmas GE, Fahrenholtz WG. Plasma arc welding of ZrB₂-20vol% ZrC ceramics. *Journal of the European Ceramic Society*. 2014;34(15):3549-3557.
9. Zhang M, Qu KL, Luo SX, Liu SS. Effect of Cr on the microstructure and properties of TiC-TiB₂ particles reinforced Fe-based composite coatings. *Surface and Coatings Technology*. 2017;316:131-137.
10. Xu J, Zou B, Zhao S, Hui Y, Huang WZ, Zhou X, et al. Fabrication and properties of ZrC-ZrB₂/Ni cermet coatings on a magnesium alloy by atmospheric plasma spraying of SHS powders. *Ceramics International*. 2014;40(10 Part A):15537-15544.
11. Zhang L, Sun D, Yu H, Li H. Characteristics of Fe-based alloy coating produced by plasma cladding process. *Materials Science and Engineering: A*. 2007;457(1-2):319-324.
12. Contin A, Alves KA, Campos RA, Vasconcelos G, Damm DD, Trava-Airoldi VJ, et al. Diamond Films on Stainless Steel Substrates with an Interlayer Applied by Laser Cladding. *Materials Research*. 2017;20(2):543-548.

13. Liu P, Zhang YB, Luo H. Surface modification of pure Ti with TiB₂/Si₃N₄ reinforced coating. *Surface Engineering*. 2011;28(7):532-535.
14. Zhang P, Wang X, Guo L, Cai L, Sun H. Characterization of in situ synthesized TiB₂ reinforcements in iron-based composite coating. *Applied Surface Science*. 2011;258(4):1592-1598.
15. Chao MJ, Wang WL, Liang EJ, Ouyang D. Microstructure and wear resistance of TaC reinforced Ni-based coating by laser cladding. *Surface and Coatings Technology*. 2008;202(10):1918-1922.
16. Meng JS, Jin G, Shi XP. Structure and tribological properties of argon arc cladding Ni-based nanocrystalline coatings. *Applied Surface Science*. 2018;431:135-142.
17. Hall EO. The Deformation and Ageing of Mild Steel: III Discussion of Results. *Proceedings of the Physical Society. Section B*. 1951;64(9):747-753.
18. Cheng EJ, Katsui H, Goto T. Microstructure of ZrB₂-ZrN directionally solidified eutectic composite by arc-melting. *Journal of Asian Ceramic Societies*. 2018;6(1):102-107.
19. Liu P, Sun S, Xu S, Li Y, Ren G. Microstructure and properties in the weld surface of friction stir welded 7050-T7451 aluminium alloys by laser shock peening. *Vacuum*. 2018;152:25-29.
20. Zhang L, Sun D, Yu H. Characteristics of plasma cladding Fe-based alloy coatings with rare earth metal elements. *Materials Science and Engineering: A*. 2007;452-453:619-624.
21. Wang XH, Zhang M, Du BS. Fabrication In Situ TiB₂-TiC-Al₂O₃ Multiple Ceramic Particles Reinforced Fe-Based Composite Coatings by Gas Tungsten Arc Welding. *Tribology Letters*. 2011;41(1):171-176.
22. Zhu YC, Yukimura K, Ding CX, Zhang PY. Tribological properties of nanostructured and conventional WC-Co coatings deposited by plasma spraying. *Thin Solid Films*. 2001;388(1-2):277-282.
23. Agarwal A, Dahotre NB. Comparative wear in titanium diboride coatings on steel using high energy density processes. *Wear*. 2000;240(1-2):144-151.
24. Zou B, Tao S, Huang W, Khan ZS, Fan X, Gu L, et al. Synthesis and characterization of in situ TiC-TiB₂ composite coatings by reactive plasma spraying on a magnesium alloy. *Applied Surface Science*. 2013;264:879-885.